Tectonophysics 890 (2024) 230496

Contents lists available at ScienceDirect

Tectonophysics

journal homepage: www.elsevier.com/locate/tecto

Crustal structure of the Bushveld complex, South Africa from 1D shear wave velocity models: Evidence for complex-wide crustal modification

Kaelie Contreras [a], Andrew Nyblade [a,b,*], Raymond Durrheim [b], Susan Webb [b], Musa Manzi [b], Islam Fadel [c]

[a] Department of Geosciences, Penn State University, University Park, PA 16802, USA
[b] School of Geosciences, University of the Witwatersrand, Private Bag 3, Johannesburg 2050, South Africa
[c] Faculty of Geo-Information Science and Earth Observation (ITC), University of Twente, Enschede, the Netherlands

ARTICLE INFO

Keywords:
Bushveld complex
Shear Wave Velocity
Crustal Structure
Moho

ABSTRACT

Thirty-nine 1D shear wave velocity profiles, obtained by jointly inverting receiver functions and Rayleigh wave group velocities, are used to investigate the crustal structure of the Bushveld Complex in northern South Africa. Data from teleseismic earthquakes recorded on broadband seismic stations between 1997 and 1999 and 2015–2020 were used to compute P-wave receiver functions. Rayleigh wave group velocities between 5 and 30 s period were obtained from an ambient noise tomography and combined with group velocities between 30 and 60 s period from a published continental-scale surface wave tomography model. Moho depths of 45–47.5 km are found under the center of the complex compared to 40 km thick crust, on average, surrounding the complex, indicating ~5–7 of crustal thickening. The bottom ~10 km or more of the lower crust across much of the Bushveld Complex has a Vs $\geq$ 4.0 km/s, consistent with a mafic composition, whereas in most areas around the margins of the complex the thickness of the mafic lower crust is much less than 10 km. In the upper crust higher velocity structure (Vs $>$ 3.6 km/s) above 15 km depth underlain by lower velocity structure is seen in many locations, suggesting the presence of mafic/ultramafic layering. These results favor the continuous-sheet model for the structure of the Bushveld Complex because the ensemble of 1D models is characterized by three diagnostic features consistent with that model: (1) thicker crust under the center of the complex than away from the complex; (2) a greater thickness of high-velocity (i.e., mafic) layering in the lower crust under the complex compared to away from the complex; (3) high-velocity (i.e., mafic/ultramafic) layering in the upper crust beneath much of the complex. The lack of upper crustal mafic/ultramafic layering beneath some parts of the complex is consistent with the post-emplacement tectonic and magmatic history of the complex.

1. Introduction

The 2.1 Ga Bushveld Complex is the largest known layered mafic intrusion on the planet (Eglington and Armstrong, 2004; Johnson et al., 2006; Webb et al., 2004; Finn et al., 2015) estimated to span ~122,000 km^2 within the northern section of the Kaapvaal Craton in South Africa (Cawthorn and Boerst, 2006) (Fig. 1). The complex consists of mafic and ultramafic lithologies that host the world's largest platinum group element reserves.

The geologic uniqueness of the complex has motivated many studies of its structure, origin and emplacement mechanisms. Although the age of the Bushveld Complex and surrounding intrusions, as well as the time interval of emplacement, are well constrained (e.g., SACS, 1980; Cheney and Twist, 1991; Buick et al., 2001; Gerya et al., 2004; Zeh et al., 2015; Basson, 2019), attempts to unravel its origin have been hindered by limited knowledge of its subsurface structure. A number of models have been proposed for how the complex formed, and include intracratonic rifting (Eriksson et al., 1991; Eriksson and Reczko, 1995; Clarke et al., 2009; Kruger, 2005), a meteorite impact (Hamilton, 1970; Rhodes and Bornhorst, 1975; Elston, 1992), magma diapirism associated with a mantle plume (Sharpe et al., 1980; Walraven, 1988; Schweitzer et al., 1997; Gibson and Stevens, 1998; Buchanan et al., 2004), and decompression melting in a back-arc setting (Willmore et al., 2002).

This study uses a new broadband seismic dataset to improve our understanding of the shear wave velocity structure of the complex and surrounding crust by jointly inverting P-wave receiver functions and

* Corresponding author at: Department of Geosciences, Penn State University, University Park, PA 16802, USA
E-mail address: aan2@psu.edu (A. Nyblade).

https://doi.org/10.1016/j.tecto.2024.230496
Received 13 November 2023; Received in revised form 23 August 2024; Accepted 1 September 2024
Available online 3 September 2024

Rayleigh wave group velocities. The Rayleigh wave group velocities come from a new ambient noise tomography of the study area as well as a published surface wave tomography model of southern Africa. Group velocity dispersion curves are used with high frequency receiver functions to obtain 1D shear velocity models of the upper crust, and with both low and high frequency receiver functions to model the lower crust and estimate crustal thickness. The 1D models are combined with similar 1D models published by Kgaswane et al. (2009) for seismic stations surrounding the Bushveld Complex to characterize further the thickness and composition of the crust and evaluate explanations for the origin of the complex.

2. Tectonic and geologic background

The Bushveld Complex lies within the northern Kaapvaal Craton and is bounded to the north by the Limpopo Belt and Zimbabwe Craton (Fig. 1a inset). The Bushveld Complex formed within the Witwatersrand and Pietersburg subterranes of the Kaapvaal Craton and intruded into and through the Paleoproterozoic Transvaal Basin (Johnson et al., 2006) (Fig. 1a). The Thabazimbi-Murchison Lineament (TML) extends for ~500 km NE – SW (Good and De Wit, 1997) through the Bushveld Complex, separating the Witwatersrand subterrane from the Pietersburg subterrane. During the Phanerozoic, much of the region was covered by Permian-Jurassic Karoo sediments and possibly basalt flows (Smith, 1990) (Fig. 1a). The Premier and Maarsfontein kimberlites erupted along the southern and northern margins of the complex, respectively, and the Palmietgat kimberlite erupted through the center of the complex (Webb et al., 2011; Zeh et al., 2015) (Fig. 1a).

2.1. Bushveld complex layering

The Bushveld Complex consists of several layers (Fig. 1a); the felsic-volcanic rocks of the Rooiberg group (~3 km thick), intrusive rocks of the Rustenberg layered suite (~7 km thick) and granites making up the Lebowa and Rashoop suites (~2 km thick) (e.g., SACS, 1980: Hatton and Schweitzer, 1995; Cawthorn and Boerst, 2006; Johnson et al., 2006; Cawthorn, 2015; Zeh et al., 2015). It has a total vertical thickness of about 8 to 12 km (Webb et al., 2004) and is comprised of four lobes: northern, eastern, western, and southeastern or southern, also known as the Bethel lobe (Cawthorn and Webb, 2001; Johnson et al., 2006) (Fig. 1a). While the lobes are predominantly comprised of mafic and granitic rocks underlain by Transvaal Supergroup sediments, the northern lobe is also in contact with Archean granite-gneiss basement (Basson, 2019).

The Rustenburg layered suite (RLS) hosts most of the mineralization within the complex, has a maximum thickness of 8 km, is comprised of norites, pyroxenites, anorthosites, harzburgites, dunites, diorites, and gabbros (Barnes et al., 2010), and is subdivided into five major zones: Marginal, Lower, Critical, Main, and Upper (Johnson et al., 2006). The Critical zone includes two layers mined for platinum, the chromitite-rich UG2 and the pyroxenite-rich Merensky Reef (Barnes et al., 2010). The RLS intruded the Rashoop Granophyre suite and the Lebowa Granite suite, which consist of tabular, coarse-grained granite and granophyric granitoids (SACS, 1980; Johnson et al., 2006). The eruption of the Rooiberg group, comprised of predominantly siliceous volcanic rocks interbedded by thin, metasedimentary strata (Eriksson et al., 1994), is suggested to have taken place prior to the formation of the RLS (Hatton and Schweitzer, 1995). For this reason, the volcanic units of the Rooiberg group are observed in the floor and roof of the intrusion (Cheney and Twist, 1991; Johnson et al., 2006). The lithology of the complex is similar within the eastern, western, far western, and northern lobes (Barnes et al., 2010), as well as the southern lobe (Cawthorn and Webb, 2001; Webb et al., 2004).

2.2. Prior geophysical studies

The crustal structure of the Bushveld Complex has been investigated by a number of geophysical studies to determine overall geometry, interlimb continuity, physical properties and emplacement history (e.g., Molengraaff, 1901; Hall, 1932; Cousins, 1959; Walraven, 1988; Meyer and De Beer, 1987; Nguuri et al., 2001; Webb et al., 2004; Nair et al., 2006; Kgaswane et al., 2009; Webb et al., 2011; Kgaswane et al., 2012; Cole et al., 2014; Finn et al., 2015, Shithigona et al., 2018). The Bushveld Complex was initially thought to have been a laccolith structure

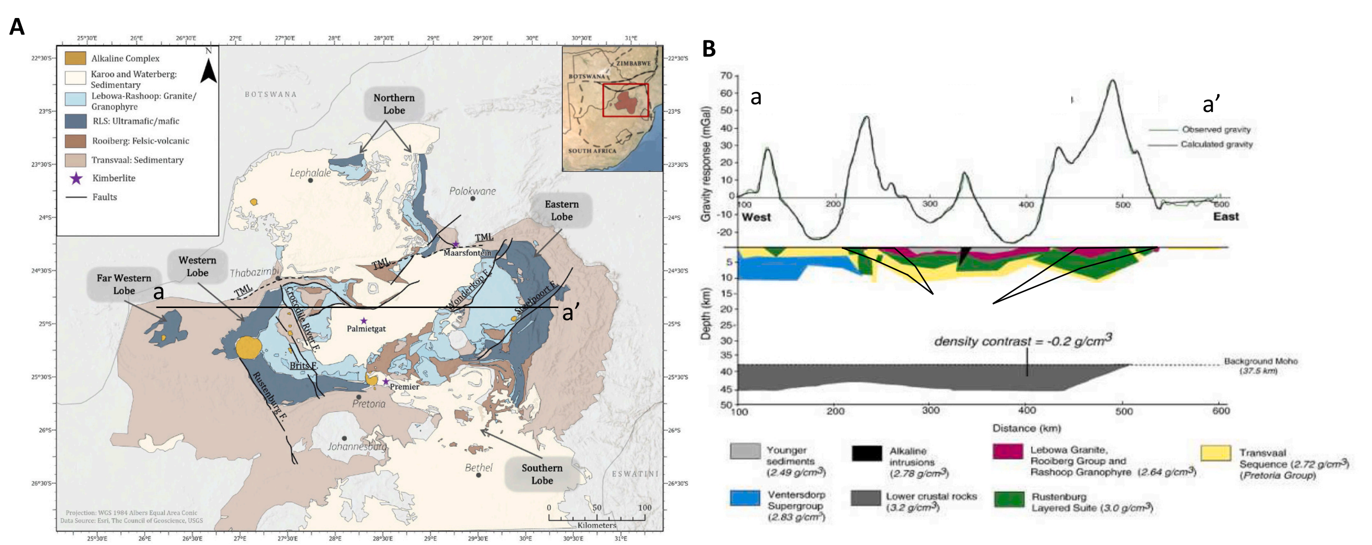

Fig. 1. A) Geologic map of the Bushveld Complex showing main lithologies, location of lobes, main faults, and kimberlites. Inset map shows the location within South Africa, with the black dashed line showing the margins of the Kaapvaal and Zimbabwe cratons. Lithologies and faults are georeferenced from the Council of Geoscience map which was compiled by M.R. Johnson and L.G. Wolmarans and prepared by C. Thomas (2008). The dashed lines show the Thabazimbi-Murchison Lineament (TML). The purple stars show locations of kimberlites (Premier, Maarsfontein, Palmietgat). a - a' show the location of the profile in B. B) West-east cross section showing Bouguer gravity on top panel and a crustal density model below, (modified from Kgaswane et al., 2012), for the continuous sheet model for the Bushveld Complex showing mafic/ultramafic layering within the upper crust extending across the complex, as proposed by Webb et al. (2004). The black polygons show the two limbs of the dipping sheet model proposed by Meyer and De Beer (1987). Thin gray lines show country boundaries. (For interpretation of the references to colour in this figure legend, the reader is referred to the web version of this article.)

that transgressed the Transvaal Basin (Molengraaff, 1901). Hall (1932) suggested a lopolith structure, and Cousins (1959), based on gravity data, suggested the complex closely resembled a structure caused by dike-like bodies, where each lobe was feed by its own magma chamber. This model was refined into a dipping-sheet model, first proposed Molyneux and Klinkert (1978) and later supported by Du Plessis and Kleywegt (1987) and Meyer and De Beer (1987), who constrained their model using electrical soundings which indicated the presence of a conductive layer at depth. Meyer and De Beer (1987) also suggested that the eastern and western lobes extend to depths of ~15 km and not are connected (Fig. 1b). They also attributed the conductive layer to sedimentary strata of the Transvaal Supergroup found underneath the outcropping lobes. More recently, a continuous-sheet model was proposed based on the gravity data suggesting that mafic layers continue at depth beneath the center of the complex connecting both the eastern and western lobes (e.g., Cawthorn et al., 1998; Cawthorn and Webb, 2001; Webb et al., 2004) (Fig. 1b). Webb et al. (2004) suggested that the conductive layer identified by Meyer and De Beer (1987) was indicative of RLS rocks based on the drilling results of Walraven (1988).

Several seismic studies have reported Moho depths beneath seismic stations located in the Bushveld Complex using a variety of modeling methods, including P-wave receiver functions, ambient noise tomography and surface wave tomography (e.g., Nguuri et al., 2001; Nair et al., 2006; Yang et al., 2008; Kgaswane et al., 2009, 2012; Youssof et al., 2013). This study builds on the results of Kgaswane et al. (2012), who used a joint inversion of receiver functions and Rayleigh wave group velocities, similar to the approach taken in Kgaswane et al. (2009). Kgaswane et al. (2012) used a total of 16 broadband seismic stations from the Southern African Seismic Experiment (SASE) network, 14 of which are also used in this study. In addition to P-wave receiver functions, Kgaswane et al. (2012) used local earthquakes recorded on the SASE network in a surface wave tomography to obtain Rayleigh wave group velocity curves for use in the joint inversion. Their results showed a maximum crustal thickness of ~45 km in the center of the complex and ~ 37–38 km outside of the complex. In the center of the complex, some stations showed shear wave velocities as high as 3.7–3.8 km/s in the upper 10 km of the crust, and greater than 5 km of high velocity (Vs ≥4.0 km/s) layering in the lower crust, which they argued supported the continuous-sheet model. The revised continuous-sheet gravity model from Kgaswane et al. (2012), modified from the Webb et al. (2004) model and constrained by their joint inversion results, shows mafic layering that is continuous in the lower and upper crust across the complex, but with substantial complexity, especially in the upper crust (Fig. 1b).

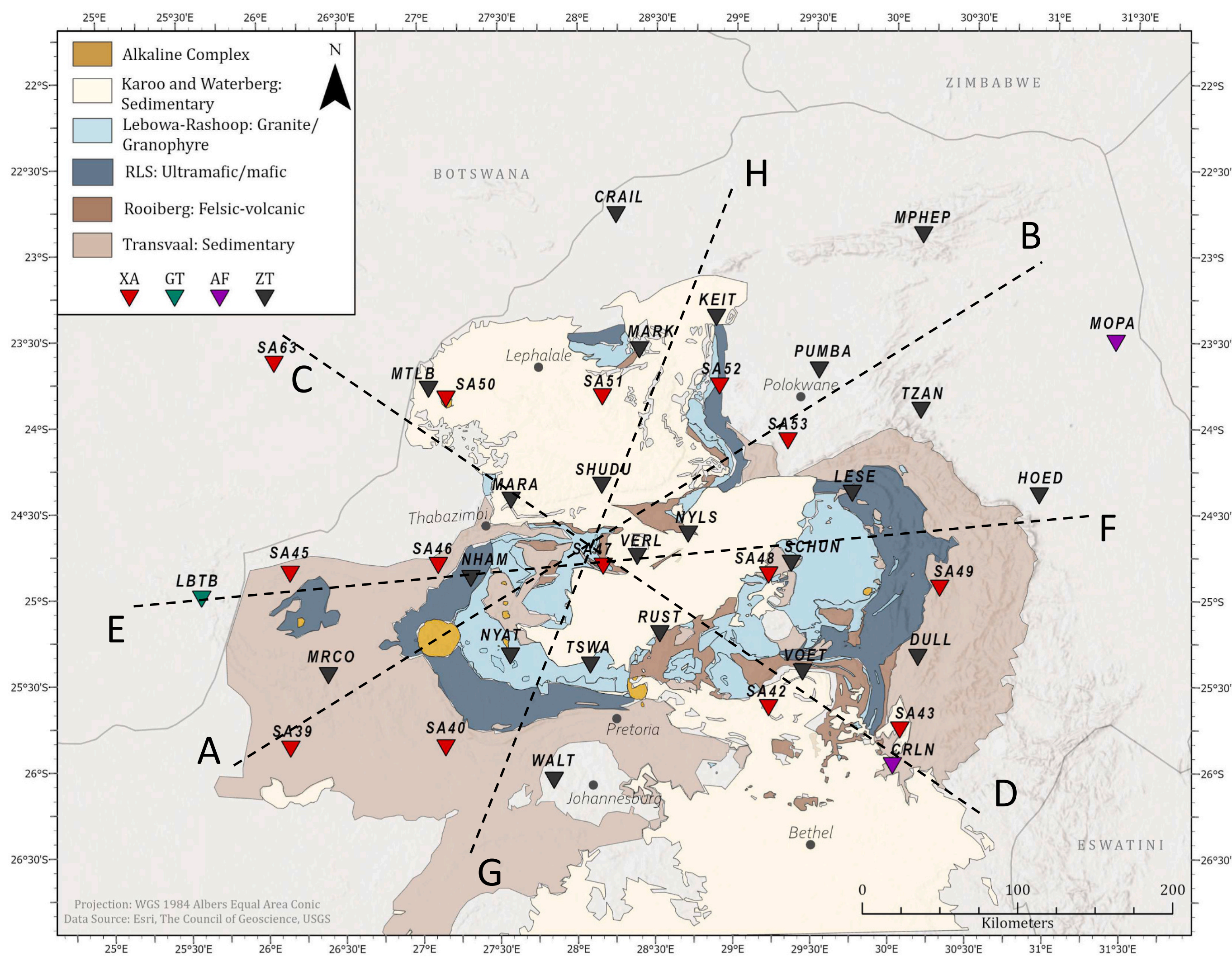

Fig. 2. Geologic map of the Bushveld Complex showing the 40 broadband seismic stations used in this study. The networks (network codes XA, GT, AF, ZT) to which the stations belong are designated by red, green, purple, and black inverted triangles. Lithologies and faults are georeferenced from the Council of Geoscience map which was compiled by M.R. Johnson and L.G. Wolmarans and prepared by C. Thomas (2008). Thin gray lines show country boundaries. (For interpretation of the references to colour in this figure legend, the reader is referred to the web version of this article.)

3. Data and methods

3.1. Data

Teleseismic earthquakes recorded on 39 broadband seismic stations were used in this study (Fig. 2). The data come from 22 temporary stations (2015–2020) belonging to the AfricaArray Bushveld network (https://doi.org/10.7914/SN/ZT_2015), two permanent stations belonging to the AfricaArray network (https://doi.org/10.7914/SN/AF), 14 temporary stations (1997–1999) belonging to the Southern African Seismic Experiment (SASE) network (https://doi.org/10.7914/SN/XA_1997), and one permanent station belonging to the Global Seismographic Network (GSN) (https://doi.org/10.7914/SN/GT). Station information is provided in Table S1.

Three thousand five hundred and fifty-five earthquakes recorded with magnitudes >5.0 and epicentral distances between 30 and 99° (Fig. S1) were used to compute receiver functions. Data from the SASE network were obtained between April 1997 and July 1999, and data from all other networks (ZT, AF, GT) were obtained from January 1st, 2015, to December 31st, 2020. Event information is provided in Table S2.

3.2. Receiver functions

Receiver functions reveal P-to-S converted energy beneath a seismic station from a velocity discontinuity (Langston, 1979). To generate receiver functions, seismograms were first detrended and tapered using a taper width of 0.02. The detrended and tapered data were then high pass filtered at 0.05 Hz and low pass filtered at 8 Hz. Next, the waveforms were down-sampled to 10 Hz and cut to 10 s before the P-wave arrival time and 110 s after the P-wave arrival time, and the horizontal traces were rotated to the great circle path to obtain radial and transverse components. Using the iterative, time domain deconvolution technique (Ligorria and Ammon, 1999), the vertical component was deconvolved from the radial and tangential components using a maximum number of 500 iterations to generate the receiver functions. Receiver functions were calculated for Gaussian width factors (α) of 2.5, and 1.0, which correspond to frequencies of $\leq$1.25 Hz, and $\leq$ 0.5 Hz, respectively.

To high grade the receiver functions, a quality control process was applied where the waveforms were convolved back with the corresponding vertical component (Ligorria and Ammon, 1999), and only those fitting 80 % or more of the observed power in the original radial component were selected for further analysis. In addition, manual inspection was applied to remove data with large amplitudes on the transverse receiver functions, unclear arrivals on the radial receiver functions, and otherwise noisy receiver functions. For stations where data were limited, specifically those from the XA network, only the manual inspection process was used. Station WTBG from the ZT network displayed large amplitudes on all transverse receiver functions and was therefore not used in this study. Examples of low (Gaussian of 1.0) and high (Gaussian of 2.5) frequency receiver functions for station NHAM are shown in Fig. 3, and the receiver functions for all stations can be found in Fig. S2.

Receiver functions were stacked by ray parameter for use in the joint inversion with Rayleigh wave group velocities. Ray parameter groups were selected to account for phase move-out resulting from varying incidence angles (Cassidy, 1992; Gurrola and Minster, 1998). For each station, the receiver functions were initially grouped from 0.04 to 0.049 s/km, 0.05 to 0.059 s/km, 0.06 to 0.069 s//km, and 0.07 to 0.079 s/km. However, the ray parameter groupings were adjusted for each station depending on the quality and quantity of receiver functions. In preparation for the joint inversion, the receiver function stacks were normalized by the area of the averaging function associated with their

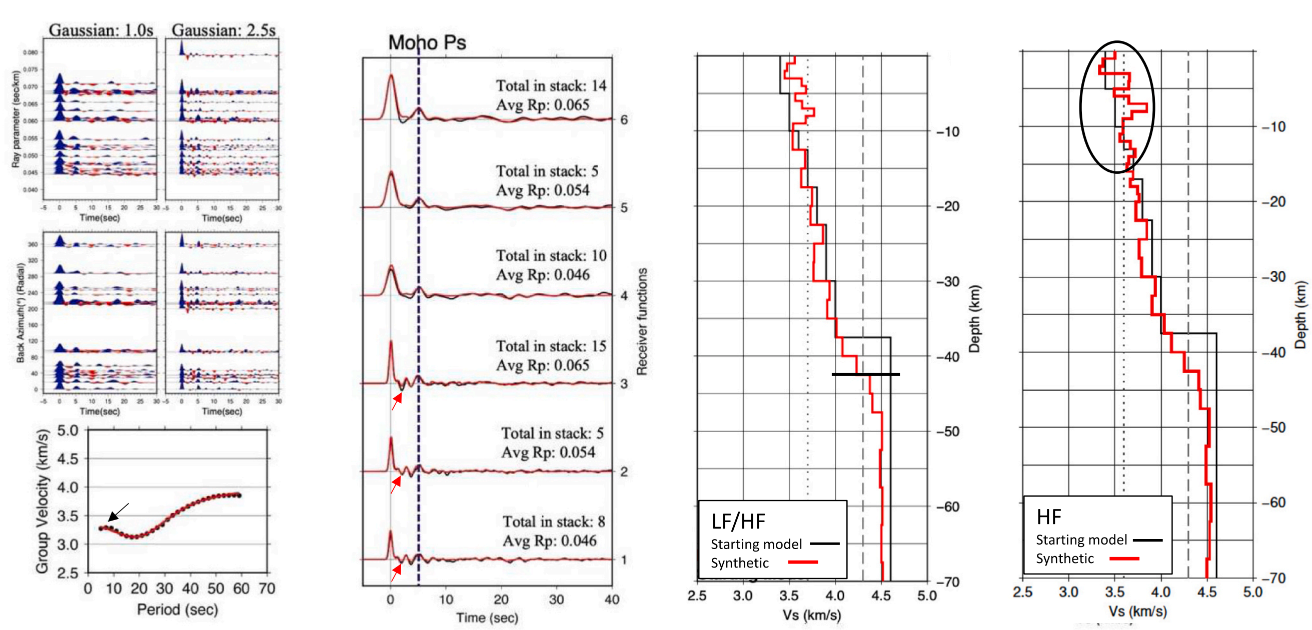

Fig. 3. (Top left) Figures showing low frequency (Gaussian 1.0) and high frequency (Gaussian 2.5) radial receiver functions displayed by back azimuth and ray parameter for station NHAM. (Bottom left) Rayleigh wave group velocity dispersion curve with observations (black dots) and model synthetic (red curve). The small black arrow shows the increase in group velocities at 5 s period indicating higher velocity layers in the upper crust. (Middle) Receiver functions (black lines) stacked by ray parameter (Rp) and model synthetics (red curves). The bottom three receiver function stacks are high frequency receiver functions, and the top three are low frequency receiver functions. The dashed line shows the Moho Ps arrival. The small red arrows show the negative arrival 1–2 s after the P-wave indicating a decrease from higher to lower velocity layers in the upper crust. (Right) Shear wave velocity models. LF/HF = model from inverting low and high frequency receiver functions. HF = model from inverting high frequency receiver functions only. The vertical dotted line indicates Vs for 3.7 km/s for LF/HF and 3.6 km/s for HF models. The vertical dashed line indicates Vs for 4.3 km/s for both models. The horizontal black line shows the Moho (42.5 km depth). High velocities in the upper crust are indicated by the oval. (For interpretation of the references to colour in this figure legend, the reader is referred to the web version of this article.)

specific Gaussian bandwidth parameter. Fig. 3 shows the receiver function stacks for station NHAM. Low and high frequency receiver function stacks for all stations can be found in the supplemental material (Figs. S3, S4).

3.3. Rayleigh wave group velocities

An ambient noise tomography was performed using data from the AfricaArray Bushveld network (network code ZT) to obtain shorter period Rayleigh wave group velocities using the processing workflow of Fadel et al. (2020) based on Poli et al. (2013). The data were pre-processed by first removing the instrument response, filtered between 1 and 50 s periods, decimated to 0.25 s, and the subjected to spectral whitening. Following Poli et al. (2013), who illustrated that stacking over several months can yield representative dispersion curves, inter-station cross-correlation measurements were carried out using 4-h segments, excluding segments with a maximum amplitude 10 times higher than the standard deviation, and then linearly stacked over a 3-month period. Following that, the automated frequency-time analysis (AFTAN) was utilized to extract interstation dispersion measurements from the cross-correlation functions using a signal-to-noise ratio threshold of 10 and the one wavelength criteria for the maximum period (Luo et al., 2015) for group velocity between 3 and 35 s (Bensen et al., 2007).

We inverted all interstation dispersion data for group velocity maps on 0.25 by 0.25 grids using the technique of Barmin et al. (2001). The tomographic inversion is governed by a misfit function depending on data misfit (path density contribution λ), model perturbation from the background model (norm damping β), and model smoothness (weight α and Gaussian smoothness width σ). We varied the different parameters in a systematic way exploring the range of possible values (200–10 for α & σ, 2.5–0.1 for β and 1–0.01 for λ) until we arrived at results that balanced the data misfit and the final smoothness. The final parameters used were $\alpha = 50, \beta = 1.0, \sigma = 50, and\ \lambda = 0.1$. A checkerboard test was carried out to confirm the 0.25-degree grid cell size provides the optimum spatial resolution (Rawlinson and Sambridge, 2003).

Ray coverage over the Bushveld Complex is shown in Fig. S5, Fig. S6 shows checkerboard resolution tests, and Fig. 4 shows the group velocity maps for periods of 5, 10, 20, and 30 s. Spatial variability in group velocities at any given period is in the range of ~0.2 km/s for areas where there is good ray coverage and resolution.

For longer periods (30–60 s), group velocities were taken from the Raveloson et al. (2015) surface wave tomography model for southern Africa. For each station, a composite Rayleigh wave group velocity curve from 5 to 60 s was constructed by combining the shorter periods from the ambient noise tomography with the longer periods from the Raveloson et al. (2015) model. The data points were smoothed with a 3-point running average to produce the curve used in the joint inversion with the receiver functions. For stations MOPA, MPHEP, and CRLN there was significant mismatch in two curves for the 30–35 s periods, which

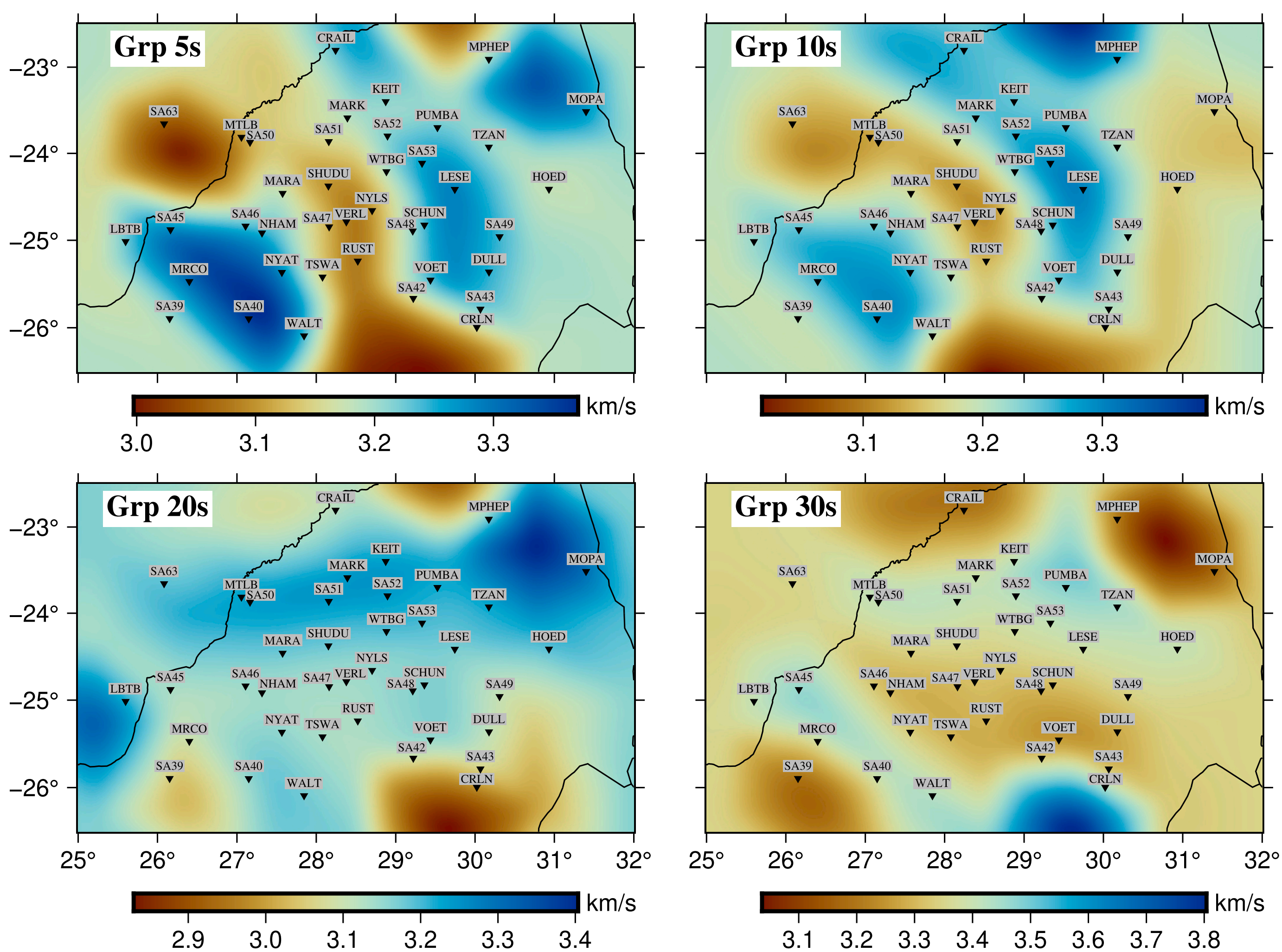

Fig. 4. Ambient noise tomography results showing Rayleigh wave group velocities for periods of 5, 10, 20, and 30 s. The black inverted triangles are seismic station with names. Black lines show country borders.

we attribute to the limited resolution of the ambient noise model along the edge of the study area where these stations are located (Fig. S5). To obtain smooth, representative dispersion curves for MOPA and MPHEP, a dispersion curve was generated by averaging of curves for nearby stations CRAIL, HOED, PUMBA, and TZAN. The dispersion curve from station SA43 was used for station CRLN.

3.4. Joint inversion

The joint inversion of receiver functions and surface wave dispersion measurements was preformed using a linearized inversion method to constrain shear-wave velocity with depth (Julia et al., 2000; Julia et al., 2003). The model contains 85 layers and extends to a depth of ~600 km. The model is parametrized with 1-km thick layers to a depth of 10 km, 2.5-km thick layers to a depth of 47.5 km, 5-km thick layers to a depth of 242.5 km, and 17 to 40-km thick layers below 242.5 km depth. The starting velocity model used in this study is identical to the model used by Kgaswane et al. (2012) that was constructed using the PREM model (Dziewonski and Anderson, 1981) modified above 60.5 km depth to better reflect the average crustal and uppermost mantle structure of the Kaapvaal Craton (Kgaswane et al., 2009) (Fig. 3). The P-wave velocities (Vp) were estimated using a Vp/Vs ratio of 1.75 for each layer. Like the approach of Kgaswane et al. (2009), the density for the starting model was determined using the empirical Vs –density relation in Brocher (2005).

An influence factor to 0.5 was used in the inversions to give equal weight to the receiver function stacks and group velocity measurements. Smoothness constraints in the inversion regularize the inversion process (Ammon et al., 1990; Julia et al., 2003). At the start of each inversion, the smoothing parameter was set to zero, and then, if the resulting model had geologically unrealistic velocities, for example, mantle-like velocities of 4.4 km/s or greater in the upper crust, or else the inversion appeared to be adding large block-by-block changes in the velocity model to fit lower amplitude higher frequency arrivals in the receiver function stacks that could be noise, the smoothing parameter was adjusted. An example of the inversion results for station NHAM using both high and low frequency receiver functions and also only high frequency receiver functions is shown in Fig. 3.

To estimate the uncertainties of the velocity models, the approach developed by Julia et al. (2000) was used, which involves repeatedly performing the inversions using a range of inversion parameters, and then examining the models to see how much Vs in any layer changes or by how much the depths of velocity discontinuities change. According to Julia et al. (2000), by repeatedly performing the inversions with a range of inversion parameters to estimate uncertainty, the issue of not having a normally distributed set of observations, which is required by many methods used to estimate uncertainty, can be circumvented. By repeatedly performing the inversions using a random selection of inversion parameters (data weighting and starting model; see Figs. S7, S8), an uncertainty of approximately 0.1–0.2 km/s for the velocity in each layer is estimated, which translates into an uncertainty of ~2–3 km in the depth of the Moho or any other velocity boundary in a model.

3.5. H–k stacking

To provide a consistency check on the joint inversion results, the *H–k* stacking method was applied to the receiver functions to obtain estimates of crustal thickness (*H*) and *Vp*/Vs (*k*) (Zhu and Kanamori, 2000). In this method, the receiver functions are transformed to the *H–k* parameter space by an objective function:

$$S(H,k) = \sum_{j=1}^{N} w_1 r_j(t_1) + w_2 r_j(t_2) - w_3 r_j(t_3) \tag{1}$$

where *ti* are the traveltimes for the three converted phase arrivals, Ps and PpPs and PsPs + PpSs, respectively, r_j, is the *j*th receiver function amplitude, *N* is the number of receiver functions and w_i are weights assigned to each phase ($\sum w_i = 1$). For a simple layer over half space model, S(*H*, *k*) is maximum when *H* and *k* obtain optimal values.

To apply the *H–k* stacking method, weights for the converted phases and an average crustal *Vp* must be selected. A *Vp* of 6.5 km/s was chosen because it is consistent with average crustal *P*-wave velocities determined from previous studies of Precambrian crust in southern Africa (Tugume et al., 2012; Kachingwe et al., 2015and references therein). For consistency with Tugume et al. (2012) and Kachingwe et al. (2015), values of $w_1 = 0.4$, $w_2 = 0.3$, $w_3 = 0.3$ were employed, which places close to equal weights on all the phases.

The *H–k* stacking method was performed using receiver functions generated with both 1.0 and 2.5 Gaussian filters for every station where there were a sufficient number of receiver functions to use a bootstrapping method to obtain formal uncertainty estimates. Results using receiver functions computed with a Gaussian filter of 1.0 are reported for all but four stations, where a Gaussian filter of 2.5 was used. For those stations, the Moho converted phases were more clearly seen at higher frequencies than at lower frequencies.

Formal uncertainties for *H* and *k* were obtained using a bootstrapping method, which involves repeating the stacking procedure 200 times with random, resampled data from the original dataset (Efron and Tibshirani, 1991). These are minimal uncertainties as additional uncertainties in *H* and *k* arise because of the choice of the average crustal *Vp*. Thus, *H–k* stacks were also computed using a *Vp* of 6.3 and 6.8 km/s to estimate the uncertainties that arise from the choice of *Vp* used for the stacking. The combination of the uncertainty estimates yields an overall uncertainty in Moho depth for each station of ~3–4 km. Poisson's ratio changes by about 0.01 across the range of *Vp* used for the stacking (i.e. 6.3–6.8 km/s).

4. Results and discussion

Joint inversion results are illustrated in Figs. 5–7 and results for individual stations are provided in Figs. S3 and S4. Figures with the results for the *H–k* stacking method are shown in Fig. S9, and Table S4 provides a comparison of results for the two methods. Moho depth uncertainty estimates for both methods are similar (~2–4 km).

Here we discuss features in the lower and upper crust that can be used to evaluate the structure of for the Bushveld Complex. Observations of Moho depths and lower crustal velocities are taken from velocity models where low frequency and high frequency receiver functions were jointly inverted together with group velocities. The combination of low frequency (longer wavelength) and high frequency (shorter wavelength) receiver functions provides good constraints on the Moho discontinuity (Owens and Zandt, 1985; Julia, 2007; Kgaswane et al., 2009). Observations of the upper crust are made using velocity models where only the high frequency receiver functions were jointly inverted with group velocities because upper crustal structure is not as well constrained by lower frequency receiver functions.

In the models, the sharpness of the Moho is influenced by the amplitude of the P-to-S conversion from the velocity discontinuity between the lower crust and upper mantle, as well as the amplitudes of the multiples (PpPs and PsPs+PpSs). For stations where the receiver functions have Moho Ps arrivals and multiples with low amplitudes, the Moho discontinuity in the velocity model is often gradational. The Moho depth for each station, influenced by the phase arrival times and group velocities, was determined at the depth where shear wave velocities are equal to or exceed 4.3 km/s, and where there is a discontinuity in the velocity structure (Kgaswane et al., 2009, 2012). Mantle lithologies are associated with shear wave velocities of ≥4.3 km/s (e.g., Christensen and Mooney, 1995; Christensen, 1996).

Velocity changes in the lower crust are mainly controlled by group velocities at periods >15 s together with the amplitude of the Moho Ps phase and its multiples. High velocities of ≥4.0 km/s in the lower crust are associated with mafic lithologies (e.g., Christensen and Mooney,

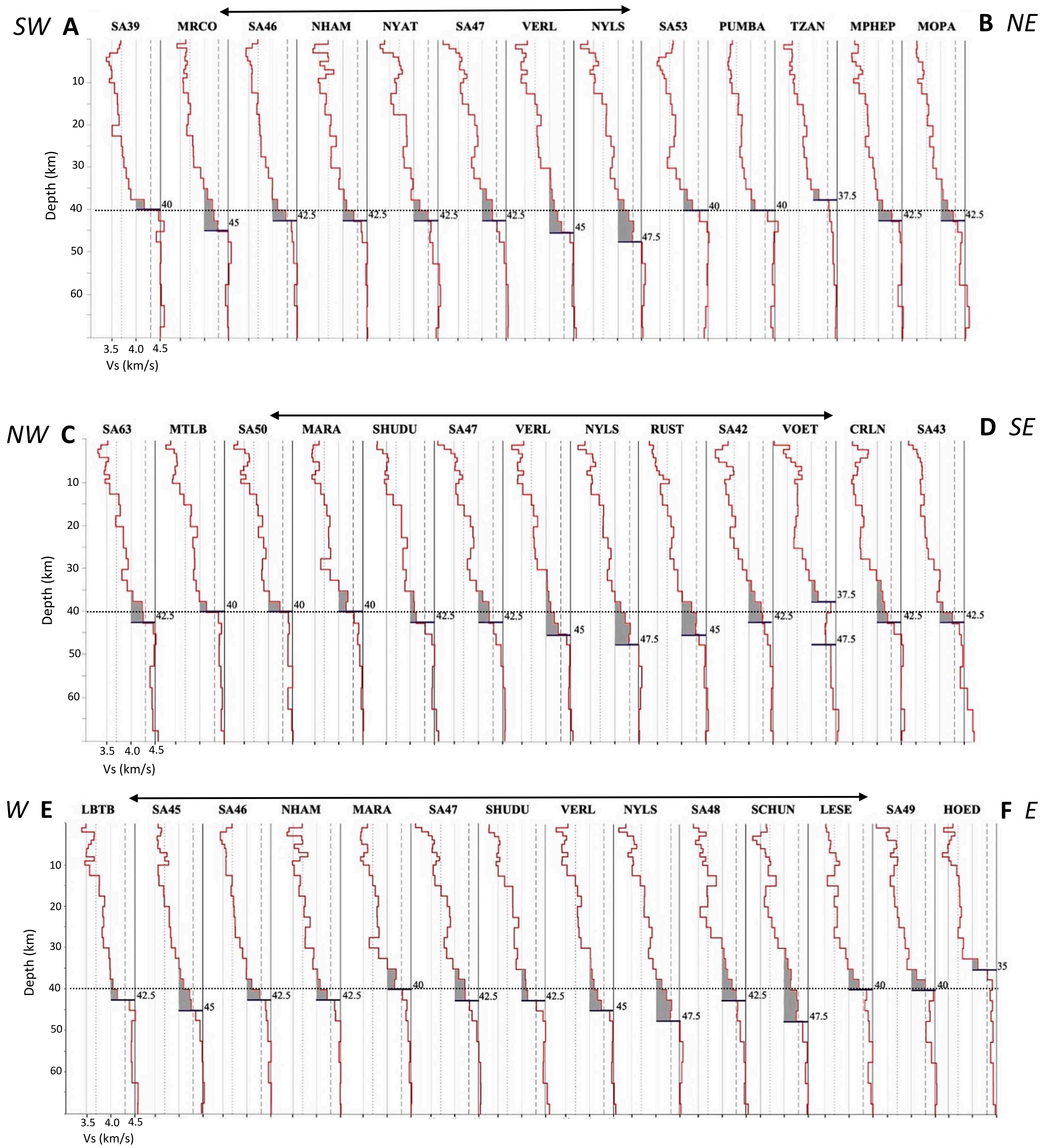

Fig. 5. Selected Vs profiles across the study area obtained from the inversion of high and low frequency receiver functions with group velocities. Profile and station locations are shown in Fig. 2. The vertical dotted line indicates a Vs of 3.7 km/s and the vertical dashed line a velocity of 4.3 km/s. The gray shaded area shows regions of the lower crust with Vs > 4.0 km/s. Bold horizontal line shows the Moho with depth given in km next to the line. The bold double arrow extends between the limbs of the Bushveld Complex. A line (dotted) is shown at 40 km depth for reference.

1995; Rudnick et al., 2003), such as amphibolites and mafic granulites.

Velocity changes in the upper crust (<~15 km depth) are primarily controlled by group velocities between periods of 5–10 s and by Ps arrivals in the first ~1–2 s of the receiver functions following the P-wave arrival. Forward modeling of the receiver functions for station SA47 by Kgaswane et al. (2012) clearly illustrated how higher velocity layers in the upper crust underlain by lower velocity layers give rise to a negative Ps arrival in the first 1–2 s of the receiver function following the P-wave arrival. Stations with Vs models showing evidence for high velocity layering underlain by low velocity in the upper crust also typically have

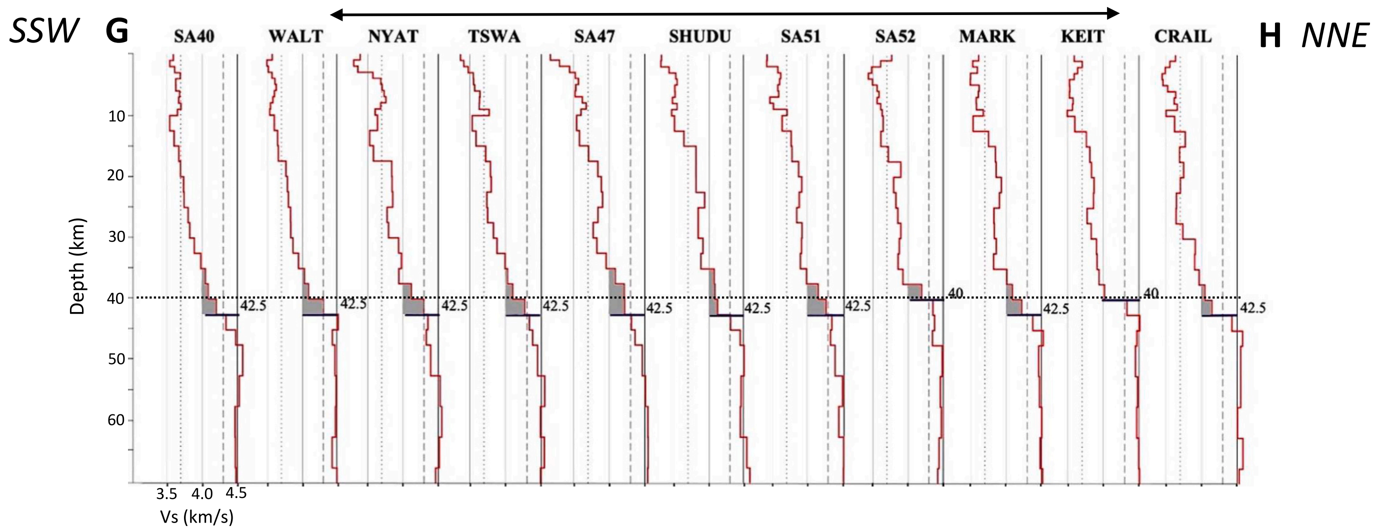

Fig. 5. (*continued*).

group velocity curves that show an increase in group velocities from 5 to10 s period along with a negative polarity Ps arrival between 1 and 2 s in the high frequency receiver functions. Following the review of velocity information on Bushveld lithologies by Kgaswane et al. (2012), a Vs of >3.6 km/s in the upper crust can be indicative of mafic lithologies within the complex. And when upper crustal layers with such higher velocities (i.e., >3.6 km/s) are underlain by lower velocity layers, this velocity pattern points to the presence of mafic layering (i.e., higher velocities) in the upper crust underlain by sedimentary or felsic igneous upper crustal lithologies (i.e., lower velocities).

Results for station NHAM are shown in Fig. 3 to illustrate Vs features in the upper and lower crust. The group velocity curve shows an "upswing" at 5 s period to ~3.3–3.4 km/s from ~3.1 km/s at periods of 15–20 s, and the high frequency receiver functions show a negative polarity arrival at about 1–2 s. The upper crust shows complicated layering where velocities alternate between ≥3.7 km/s and ≤ 3.6 km/s followed by a lower velocity zone with Vs = 3.5 km/s at 9–10 km depth, which is consistent with the presence of mafic lithologies underlain by sedimentary and/or felsic igneous lithologies. The velocity model shows a step increase in velocity (i.e., a discontinuity) at a depth of 42.5 km where the shear wave velocity exceeds 4.3 km/s, which is interpreted to be the Moho. The lower crust shows layers about 7.5 km thick immediately above the Moho that have Vs ≥ 4.0 km/s (between depths of 35 km and 42.5 km), which are interpreted as mafic lithologies in the lower crust.

4.1. Crustal thickness

Fig. 5 shows the ensemble of 1D shear wave velocity generated using both high and low frequency receiver functions arranged in profiles crossing the Bushveld Complex. Profile and station locations are shown in Fig. 2. Three of the profiles have orientations similar to the profiles in Kgaswane et al. (2012). Beneath most stations, a clear Moho discontinuity is observed, but for a number of stations (SA42, SA47, SA48, SA49, HOED, MARA, MPHEP, MRCO, NYLS, NYAT, RUST, SCHUN, SHUDU, VERL, and WALT) a gradational Moho is observed, where a Vs of ~4.2 to 4.3 km/s extends over a depth interval of ~5 km or more before Vs increases to >4.3 km/s. And for station VOET, the shear wave velocity changes from >4.3 km/s to <4.3 km/s and then finally >4.3 km/s, displaying two possible Moho locations 10 km apart.

Fig. 7a shows Moho depths obtained from this study together with results from Kgaswane et al. (2009) for stations surrounding the Bushveld Complex. Within the Bushveld Complex, Moho depths range from 35 to 45 km for all but two stations, NYLS and SCHUN, where the Moho is at a depth of 47.5 km. A Moho depth at 42.5 km is observed beneath many stations, and deeper depths (>42.5 km) observed at six stations. The deepest Moho depths (~45–47.5 km) are in the western lobe and center of the complex.

To determine the extent of crustal thickening, estimates of Moho depths from stations around the boundary of the complex are used to establish an average crustal thickness away from the complex (Fig. 7a). Stations to the south of the complex (SA31, SA32, SA33, SA34, SA35, SA36) have an average Moho depth of ~37.8 km, while stations to the north (SA55, SA56, SA57, SA64, SA65, CRAIL, MPHEP) have an average Moho depth of 41.8 km. If Moho depths from these stations are combined with those to the east (TZAN, SA54, HOED, MOPA, PUMBA) of ~38.1 km and to the west (SA38, SA39, SA60, SA62, SA63, LBTB) of 40.7 km, then the average Moho depth away from the complex is 39.6 km. This is similar to results from Kgaswane et al. (2012), who reported an average Moho depth of ~37–38 km outside of the complex, and the comparison indicates that under parts of the Bushveld Complex the crust has been thickened by up to ~5–7 km.

The deepest Moho depths reported by several other studies also have been for the center of the complex (e.g., ~45-50 km by Youssof et al., 2013; ~44-45 km by Kgaswane et al., 2012; ~47-49 km Nair et al., 2006; ~50 km Webb et al., 2004). Some of these studies show depths in the center of the complex similar to Moho depths in the western lobe (Kgaswane et al., 2012; Nguuri et al., 2001), while others show that Moho depths in the center of the complex are most similar to those in the eastern lobe (Youssof et al., 2013; Kgaswane et al., 2009; Nair et al., 2006). And one study suggests that the Moho depths in the central, western, and eastern lobes are comparable (Yang et al., 2008). The results of this study, although overall showing slightly thinner crust with more spatial variability compared to some of these previous studies, are consistent with results in the previously published studies cited above considering uncertainties in the reported Moho depths.

4.2. Lower crustal structure

For all stations used in this study, the lower crust shows at least 2.5 km of layering above the Moho with shear wave velocities ≥4.0 km/s (Fig. 5). Fig. 7b shows a map these results combined with those from Kgaswane et al. (2009). A region with greater amounts of high (≥4.0 km/s) Vs layering (~ > 10 km) can be seen in the western lobe and the center of the complex, consistent with where the thickest crust is found (Fig. 7a). The average thickness of the high Vs layers in the lower crust beneath the center of the complex (LESE, NHAM, NYAT, RUST, SA47, SA48, SCHUN, TSWA, VERL) is 9.5 km, compared to 5.8 km outside the

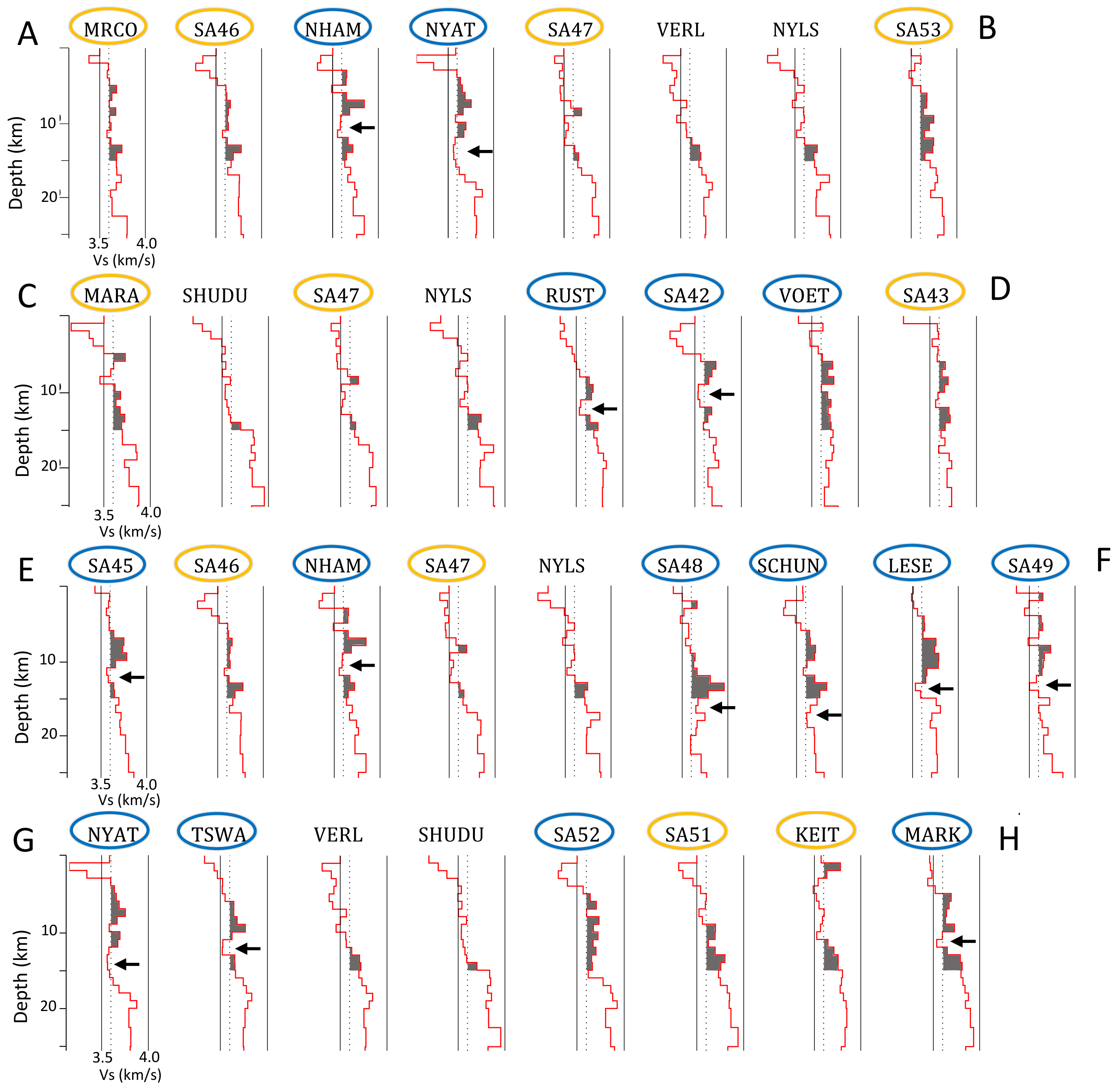

Fig. 6. Selected Vs profiles of the upper 25 km of the crust from the inversion of high frequency receiver functions only with group velocities. Profile and station locations are shown in Fig. 2. The vertical dotted line indicates Vs of 3.6 km/s. Layers with Vs > 3.6 km/s are shaded. Blue ellipses indicate stations with high velocity upper crust (Vs > 3.6 km/s) underlain by a low velocity zone. Yellow ellipses indicate stations where there possibly is one or more high velocity layers underlain by a low velocity zone. Blue and yellow colour scheme is the same as in Fig. 7c. Black arrows denote lower velocity layers below higher velocity layers. (For interpretation of the references to colour in this figure legend, the reader is referred to the web version of this article.)

center of complex. Two exceptions are stations MOPA and SA36, both well away from the Bushveld Complex. The distribution of high Vs layers in the lower crust is consistent with results from Kgaswane et al. (2012), who reported that for most stations within the complex there was high velocity layering in the lower crust exceeding a thickness of 5 km.

4.3. Upper crustal structure

Fig. 6 shows shear wave velocity profiles generated using only the high frequency receiver functions to better image upper crustal structure. As reviewed above, and summarized in Table S3, there are two features in the data that lead to high velocity layering in the models, 1) an increase in group velocity at ~5 s period to ~3.3–3.4 km/s, and 2) a negative arrival in the receiver function at 1–2 s after the P-wave arrival. In Fig. 6, stations with a higher velocity zone (i.e., layers with Vs ≥3.6 km/s) underlain by a lower velocity zone are indicated by blue ellipses. Yellow ellipses show stations where higher velocity layers may be present, but they are not as prominent as stations with blue ellipses and the higher velocity layers are not as clearly underlain by a lower velocity zone. Fig. 7c shows a map of these stations similarly colour coded. The presence of high velocity upper crustal layering is present at many station locations. However, the Vs models for stations VERL, SHUDU, NYLS

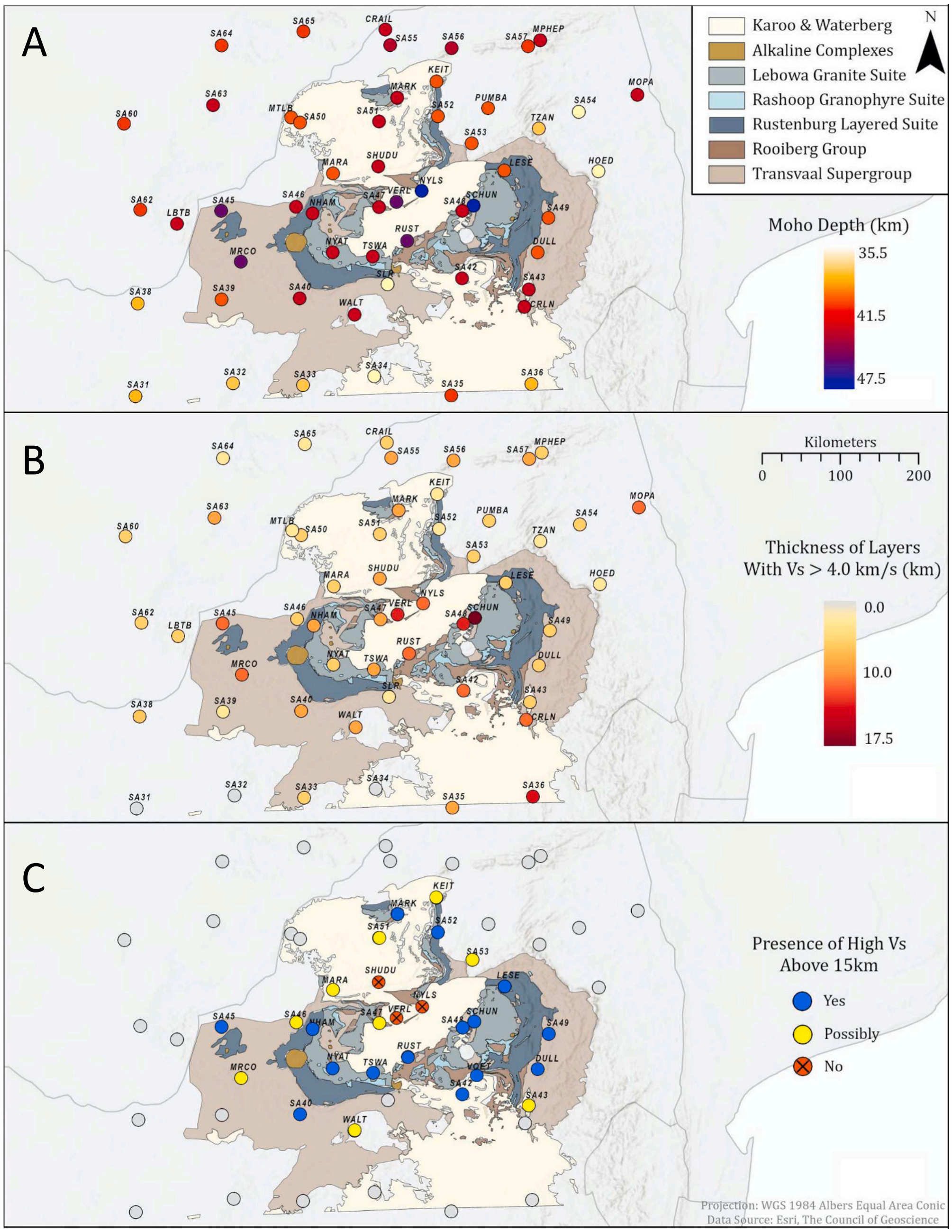

Fig. 7. Geological maps showing: (a) the distribution of crustal thicknesses across the Bushveld Complex for all stations, including those reported in Kgaswane et al. (2009); (b) the thickness of layers in the lower crust with Vs ³ 4.0 km/s for all stations, including those reported in Kgaswane et al. (2009); (c) stations with the presence of 2 or more layers in the upper crust (above 15 km depth) with Vs > 3.6 km/s underlain by model layers with lower velocities for the 39 stations used in this study. Colour coding of symbols is the same as station coding in Fig. 6.

do not show any high velocity layering (Vs > 3.6 km/s is found only at depths of 13–15 km). High Vs layering in the upper crust is more widespread across the complex than where deep Moho depths and thick layering of high Vs in the lower crust are observed. Station SA45, MRCO, and SCHUN are the only stations that have Moho depths ≥45 km, high-velocity lower crustal layers ≥10 km thick, and the presence of high velocities in the upper 15 km of the crust. The distribution of high velocities in the upper crust found in this study is consistent with the upper crustal structure reported by Kgaswane et al. (2012), who used a subset of the stations used in this study.

4.4. Evaluating the dipping and continuous-sheet models for the Bushveld complex

To evaluate the dipping and continuous-sheet models for the subsurface geometry of the Bushveld Complex, three diagnostic features of the crust can be used: (1) the presence of thicker crust beneath the complex, (2) high velocity layers in the lower crust indicating the presence of mafic rock, and (3) higher velocity layers in the upper crust underlain by a lower velocity region indicating the presence of mafic/ultramafic rock. The dipping sheet model does not predict thickened crust with mafic lower crustal lithologies beneath the center of the complex, whereas the continuous-sheet model does (Fig. 1b). Similarly, the dipping sheet model does not predict higher velocity layers in the upper crust within the center of the complex indicative of mafic/ultramafic lithologies, whereas the continuous-sheet model does. (Fig. 1b).

The results of this study, overall, support the continuous-sheet model and not the dipping sheet model because there is evidence in the ensemble of 1D shear velocity models for thickened crust, as well as mafic lithologies in both the upper and lower crust, across much of the Bushveld Complex. The crust is ~5–7 km thicker towards the center of the complex than in nearby areas around the complex. This amount of crustal thickening is consistent with the crustal density models of Webb et al. (2004) and Kgaswane et al. (2012) (Fig. 1b). Vs models for stations in the center of the complex also show thicker high-velocity layering in the lower crust, again, consistent with the continuous-sheet crustal density models of Webb et al. (2004) and Kgaswane et al. (2012) showing high density mafic lower crust under the center of the complex (Fig. 1b). In addition, high velocity upper crust layering indicating the presence of mafic lithologies is present throughout much of the complex.

Although the results of this study support the continuous-sheet model, the Vs models reveal complex upper crustal structure in several areas, consistent with reports by other studies (Kgaswane et al., 2009, 2012; Cole et al., 2014). The location of the areas with complicated upper crustal structure (stations SA47, VERL, NYLS, MARA, RUST, SA48, SA50, SCHUN, NHAM, NYAT, TSWA) are predominately in the center of the complex near complicated fault and shear zones (Fig. 1a). The location of alkaline complexes near these stations, as well as the kimberlites (Fig. 1a), also point to the possible disruption or modification of much of the upper crustal structure from post-emplacement magmatic and tectonic activity (Frick and Walraven, 1985; Webb et al., 2004). Thus, while the results of this study support the continuous-sheet model, the upper crustal layering is not uniformly thick, and in some places, locally, may not be present at all.

Our findings extend significantly beyond the results presented in Kgaswane et al. (2012). In that paper, 1D Vs models were reported for only eight stations within the Bushveld Complex, compared to results for 24 stations in this study. In addition, the group velocity model used in this study derived from ambient noise has superior resolution to the one used by Kgaswane et al. (2012). In particular, our group velocity model provides improved constraints on upper crustal velocities. For example, the group velocity curves used by Kgaswane et al. (2012) do not show the increase in velocity at ~5 s period to 3.3 to 3.4 km/s that is seen in many of the dispersion curves from the model used in this study. While the results presented by Kgaswane et al. (2012) suggested the presence of thickened crust under the complex and mafic/ultramafic layers within the upper crust, the sparse number of stations used in that study left open the question of how continuous those features were across the entire complex. The results from this study, using many more stations and an improved group velocity model, shows definitively the continuity of the thickened lower crust, the thickness of mafic lithologies in the lower crust, and the extent to which much of the upper curst contains high velocity layers indicative of mafic/ultramafic layering.

The results of this study also suggest the mafic/ultramafic layering of the Bushveld Complex could possibly be present in areas immediately surrounding outcrops of the western and eastern lobes. Stations SA45, MRCO, SA40, WALT, SA49, DULL, and SA43 show some evidence for mafic upper crustal layering, and some of these stations also show thickened crust with 10 or more kms of high-velocity lower crust, which may reflect sills associated with the complex that extend upwards of 50 km beyond the complex. Consequently, the spatial extent of the complex, as expressed in the structure of the upper and lower crust, may be larger than indicated by the outcrop pattern.

5. Summary and conclusions

In summary, receiver function stacks and Rayleigh wave group velocities for 39 seismic stations spread across and around the Bushveld Complex have been jointly inverted to obtain 1D Vs models of the crust. Moho depths of 45–47.5 km are found beneath several stations in the center of the complex compared to ~40 km thick crust, on average, surrounding the complex, indicating ~5–7 km of crustal thickening. The 1D Vs models also reveal the bottom ~10 km or more of the lower crust across much of the Bushveld Complex has a mafic composition, indicated by a Vs $\geq$ 4.0 km/s. In comparison, for most areas around the margins of the complex the thickness of the mafic lower crust is much less than 10 km. In addition, the 1D Vs models image an upper crust in many parts of the complex with higher velocity layers above 15 km depth underlain by lower velocity layers. The higher velocity upper crustal layers indicate the presence of mafic/ultramafic layering present in many areas of the complex, but not everywhere. 1D Vs models for some stations immediately surrounding the complex also suggest the presence of mafic/ultramafic layering in the upper crust and mafic layering in the lower crust, and if confirmed, this finding would indicate that the complex could have a larger spatial footprint than indicated by the outcrop pattern.

These findings favor the continuous-sheet model for the structure of the Bushveld Complex because they include three diagnostic features that are consistent with the continuous sheet model: (1) thicker crust under the center of the complex than away from the complex; (2) a greater thickness of high-velocity (mafic) layering in the lower crust compared to away from the complex; (3) high-velocity (mafic/ultramafic) layering in the upper crust present beneath most of the complex. However, the lack of mafic/ultramafic layering beneath some stations within the complex suggests the complex may have been modified by post-emplacement tectonic and magmatic activity.

There have been several models proposed for how the Bushveld Complex formed, including mantle plumes, meteorite impacts, and rifting. The findings of this study supporting the continuous-sheet model for the structure of the complex suggests the complex formed from a single large magmatic system spanning more than 400 km and not by several smaller magmatic systems. Such a large magmatic system that could modify both lower and upper crustal structure similarly over such a large region is difficult to envision in a continental rift setting or to have formed from a meteorite impact, given our understanding of rifting processes in East Africa and other regions, and the size of impact craters. A very large mantle plume or a large subduction zone magma chamber may therefore be a more likely mechanisms to have formed the Bushveld Complex.

CRediT authorship contribution statement

Kaelie Contreras: Writing – original draft, Methodology, Investigation, Formal analysis. **Andrew Nyblade:** Writing – review & editing, Writing – original draft, Project administration, Methodology, Investigation, Conceptualization. **Raymond Durrheim:** Writing – review & editing, Funding acquisition, Data curation, Conceptualization. **Susan Webb:** Writing – review & editing, Conceptualization. **Musa Manzi:** Data curation, Conceptualization. **Islam Fadel:** Visualization, Methodology, Investigation.

Declaration of competing interest

The authors declare that they have no known competing financial interests or personal relationships that could have appeared to influence the work reported in this paper.

Data availability

All data used in this study are available from the IRIS Data Management Center (http://ds.iris.edu) using the network codes provided in Section 3.1.

Acknowledgements

This work was supported by National Science Foundation grants

0440032, 0530062, 0824781, 1128936, and 1634108. R.J.D. acknowledges support from the DST/NRF South African Research Chair program. We also acknowledge the efforts of staff in the seismology group at the Council for Geosciences for installing and maintaining seismic stations in the Bushveld Complex. We would like to thank two anonymous reviewers for helpful and constructive comments.

Appendix A. Supplementary data

Supplementary data to this article can be found online at https://doi.org/10.1016/j.tecto.2024.230496.

References

Ammon, C.J., Randall, G.E., Zandt, G., 1990. On the nonuniqueness of receiver function inversions. J. Geophys. Res. 95, 15303–15318.

Barmin, M.P., Ritzwoller, M.H., Levshin, A.L., 2001. A fast and reliable method for surface wave tomography. In: Monitoring the Comprehensive Nuclear-Test-Ban Treaty: Surface Waves, pp. 1351–1375.

Barnes, S.-J., Maier, W., Curl, E., 2010. Composition of the marginal rocks and sills of the rustenburg layered suite, Bushveld Complex, South Africa: implications for the formation of the platinum-group element deposits. Econ. Geol. 105 (8), 1491–1511.

Basson, I.J., 2019. Cumulative deformation and original geometry of the Bushveld Complex. Tectonophysics 750, 177–202.

Bensen, G.D., Ritzwoller, M.H., Barmin, M.P., Levshin, A.L., Lin, F., Moschetti, M.P., Yang, Y., 2007. Processing seismic ambient noise data to obtain reliable broad-band surface wave dispersion measurements. Geophys. J. Int. 169 (3), 1239–1260.

Brocher, T. M. (2005). Empirical relations between elastic wavespeeds and density in the earth's crust. Bull. Seismol. Soc. Am., 95(6), 2081–2092. https://doi.org/https://doi.org/10.1785/0120050077.

Buchanan, P., Reimold, W., Koeberl, C., Kruger, F., 2004. Rb-Sr and Sm-Nd isotopic compositions of the Rooiberg Group, South Africa: early Bushveld-related volcanism. Lithos 373–388.

Buick, I., Maas, R., Gibson, R., 2001. Precise U-Pb titanite age constraints on the emplacement of the Bushveld Complex, South Africa. J. Geol. Soc. 158 (1), 3–6.

Cassidy, J.F., 1992. Numerical experiments in broadband receiver function analysis. Bull. Seismol. Soc. Am. 1453–1474.

Cawthorn, R. G. (2015). The Bushveld complex, South Africa. In B. Charlier, O. Namur, R. Latypov, & C. Tegner, Layered Intrusions. Springer Geology (pp. 517-587). Springer, Dordrecht.

Cawthorn, R., Boerst, K., 2006. Origin of the pegmatitic pyroxenite in the merensky unit, Bushveld Complex, South Africa. J. Petrol. 47 (8), 1509–1530.

Cawthorn, R.G., Webb, S.J., 2001. Connectivity between the western and eastern limbs of the Bushveld Complex. Tectonophysics 330 (3–4), 195–209.

Cawthorn, R.G., Cooper, G.R.J., Webb, S.J., 1998. Connectivity between the western and eastern limbs of the Bushveld Complex. S. Afr. J. Geol. 101, 291–298.

Cheney, E.S., Twist, D., 1991. The conformable emplacement of the Bushveld Mafic rocks along a regional unconformity in the transvaal succession of South Africa. Precambrian Res. 52, 115–132.

Christensen, N.I., 1996. Poisson's ratio and crustal seismology. J. Geophys. Res. Solid Earth 101 (B2), 3139–3156.

Christensen, N., Mooney, W.D., 1995. Seismic velocity structure and crustal composition of the continental crust: a global view. J. Geophys. Res. Solid Earth 100 (B6), 9761–9788.

Clarke, B., Uken, R., Reinhardt, J., 2009. Structural and compositional constraints on the emplacement of the Bushveld Complex, South Africa. Lithos 21–36.

Cole, J., Webb, S.J., Finn, C.A., 2014. Gravity models of the Bushveld Complex - have we come full circle? J. Afr. Earth Sci. 92, 97–118.

Cousins, C.A., 1959. The structure of the mafic portion of the Bushveld igneous complex. S. Afr. J. Geol. 62 (1), 179–201.

Du Plessis, A., Kleywegt, R.J., 1987. A dipping sheet model for the mafic lobes of the Bushveld Complex. S. Afr. J. Geol. 90, 1–6.

Dziewonski, A., Anderson, D., 1981. Preliminary reference Earth model. Phys. Earth Planet. Inter. 25 (4), 297–356.

Efron, B., Tibshirani, R., 1991. Statistical data analysis in computer age. Science 253, 390–395.

Eglington, B.M., Armstrong, R.A., 2004. The Kaapvaal Craton and adjacent orogens, southern Africa: a geochronological database and overview of the geological development of the craton. S. Afr. J. Geol. 107 (1–2), 13–32.

Elston, W., 1992. Does the Bushveld-Vredefort system (South Africa) record the largest known terrestrial impact catastrophe? Large Meteorite Impacts Planet. Evol. 23.

Eriksson, P., Reczko, B., 1995. The sedimentary and tectonic setting of the transvaal supergroup floor rocks to the Bushveld complex. J. Afr. Earth Sci. 21 (4), 487–504.

Eriksson, P., Schreiber, U., van der Neut, M., 1991. A review of the sedimentology of the early proterozoic pretoria group, transvaal sequence, South Africa: implications for tectonic setting. J. Afr. Earth Sci. 13 (1), 107–119.

Eriksson, P., Schreiber, U., Reczko, B., Snyman, C., 1994. Petrography and geochemistry of sandstones interbedded with the Rooiberg Felsite Group (Transvaal Sequence, South Africa); implications for provenance and tectonic setting. J. Sediment. Res. 836–846.

Fadel, I., Paulssen, H., van der Meijde, M., Kwadiba, M., Ntibinyane, O., Nyblade, A., Durrheim, R., 2020. Crustal and upper mantle shear wave velocity structure of Botswana: the 3 April 2017 central Botswana earthquake linked to the East African Rift System. Geophys. Res. Lett. 47 (4), e2019GL085598.

Finn, C.A., Bedrosian, P.A., Cole, J.C., Khoza, T.D., Webb, S.J., 2015. Mapping the 3D extent of the Northern Lobe of the Bushveld layered mafic intrusion from geophysical data. Precambrian Res. 268, 279–294.

Frick, C., Walraven, F., 1985. The petrology and geochemistry of the pre-Karoo Elandskraal Volcano, South Africa. Verhandelinge van die Geol. Vereniging van Suid-Afrika 88 (2), 225–243.

Gerya, T.V., Uken, R., Reinhardt, J., Watkeys, M.K., Maresch, W.V., Clarke, B.M., 2004. Cold diapirs triggered by intrusion of the Bushveld Complex: insight from two-dimensional numerical modeling. In: Gneiss Domes in Orogeny, 380. Geological Society of America - Special Papers, pp. 117–128.

Gibson, R., Stevens, G., 1998. Regional Metamorphism Due to Anorogenic Intracratonic Magmatism. Geological Society, London, Special Publications, pp. 121–135.

Good, N., De Wit, M.J., 1997. The thabazimbi-murchison lineament of the Kaapvaal Craton, South Africa: 2700 Ma of episodic deformation. J. Geol. Soc. 154 (1), 93–97.

Gurrola, H., Minster, J., 1998. Thickness estimates of the upper-mantle transition zone from bootstrapped velocity spectrum stacks of receiver functions. Geophys. J. Int. 133, 31–43.

Hall, A.L., 1932. The Bushveld Igneous Complex of the Central Transvaal, 28.

Hamilton, W., 1970. Bushveld complex - product of impacts?. In: Symposium on the Bushveld igneous complex and other layered intrusions, 1. Geological Society of South Africa Special Paper, pp. 367–379.

Hatton, C., Schweitzer, J., 1995. Evidence for synchronous extrusive and intrusive Bushveld magmatism. J. Afr. Earth Sci. 579–594.

Johnson, M.R., Anhaeusser, C.R., Thomas, R.J., 2006. The Geology of South Africa. Geological Society of South Africa.

Julia, J., 2007. Constraining velocity and density constrasts across the crust-mantle boundary with receiver function amplitudes. Geophys. J. Int. 171 (1), 286–301.

Julia, J., Ammon, C., Herrmann, R., Corrieg, A., 2000. Joint Inversion of receiver function and surface wave dispersion observations. Geophys. J. Int. 143 (1), 99–112.

Julia, J., Ammon, C., Herrmann, R., 2003. Lithospheric structure of the Arabian Shield from the joint inversion of receiver functions and surface-wave group velocities. Tectonophysics 371 (1-4), 1–21.

Kachingwe, M., Nyblade, A., Julia, J., 2015. Crustal structure of Precambrian terranes in the southern African subcontinent with implications for secular variation in crustal genesis. Geophys. J. Int. 202, 533–547.

Kgaswane, E.M., Nyblade, A.A., Julia, J., Dirks, P.H., Durrheim, R.J., Pasyanos, M.E., 2009. Shear wave velocity structure of the lower crust in southern Africa: evidence for compositional heterogeneity within Archaean and Proterozoic terrains. J. Geophys. Res. 114 (B12).

Kgaswane, E.M., Nyblade, A.A., Durrheim, R.J., Julia, J., Dirks, P.H., Webb, S.J., 2012. Shear wave velocity structure of the Bushveld Complex, South Africa. Tectonophysics 554-557, 83–104.

Kruger, F., 2005. Filling the Bushveld Complex magma chamber: lateral expansion, roof and floor interaction, magmatic unconformities, and the formation of giant chromitite, PGE and Ti-V-magnetite deposits. Mineral. Deposita 40, 451–472.

Langston, C., 1979. Structure under Mount Rainier, Washington, inferred from teleseismic body waves. J. Geophys. Res. 84 (B9), 4749–4762.

Ligorria, J., Ammon, C., 1999. Iterative deconvolution and receiver function estimation. Bull. Seismol. Soc. Am. 89, 1359–1400.

Luo, Y, Yang, Y, Xu, Y., Xu, H., Zhao, K., Wang, K., 2015. On the limitations of interstation distances in ambient noise tomography. Geophys. J. Int. 201, 652–661. https://doi.org/10.1093/gji/ggv043.

Meyer, R., De Beer, J.H., 1987. Structure of the Bushveld complex from resistivity measurements. Nature 325, 610–612.

Molengraaff, G., 1901. Geologie de la Republique S. Africaine. Bull. Geol. Soc. South Afr. 1, 13–92.

Molyneux, T.G., Klinkert, P.S., 1978. A structural interpretation of part of the Eastern Mafic Lobe of the Bushveld complex and its surrounds. Trans. Geol. Soc. S. Afr. 81, 359–368.

Nair, S.K., Gao, S.S., Liu, K.H., Silver, P.G., 2006. Southern African crustal evolution and composition: constraints from receiver function studies. J. Geophys. Res. 111 (B2).

Nguuri, T.K., Gore, J., James, D.E., Webb, S.J., Wright, C., Zengeni, T.G., Snoke, J.A., 2001. Crustal structure beneath southern Africa and its implications for the formation and evolution of the Kaapvaal and Zimbabwe cratons. Geophys. Res. Lett. 28 (13), 2501–2504.

Owens, T., Zandt, G., 1985. The response of the continental crust-Mantle boundary observed on broadband teleseismic receiver functions. Geophys. Res. Lett. 12 (10), 705–708.

Poli, P., Pedersen, H.A., Campillo, M., POLENET/LAPNET Working Group, 2013. Noise directivity and group velocity tomography in a region with small velocity contrasts: the northern Baltic shield. Geophys. J. Int. 192 (1), 413–424.

Raveloson, R., Nyblade, A.A., Fishwick, S., Mangongolo, A., Master, S., 2015. The upper mantle seismic velocity structure of south-central Africa and the seismic architecture of Precambrian lithosphere beneath the Congo Basin. In: de Wit, M.J., Guillocheau, F. (Eds.), The Geology and Resource Potential of the Congo Basin. Springer-Verlag. https://doi.org/10.1007/978-3-642-29482-2_1.

Rawlinson, N., Sambridge, M., 2003. Seismic traveltime tomography of the crust and lithosphere. Adv. Geophys. 46, 81–199.

Rhodes, R., Bornhorst, T., 1975. Application of discriminant function analysis to the felsic rocks of the Bushveld complex, South Africa. Lithos 193–197.

Rudnick, R., Gao, S., Holland, H., Turekian, K., 2003. Composition of the continental crust. In: The Crust, 3, p. 659.

SACS, 1980. Stratigraphy of Southern Africa. Part 1. lithostratigraphy of South Africa, South West Africa/Namibia, and the republics of Boputhatswana, Transkei and Venda. Geol. Survey South Africa Handb. 690.
Schweitzer, J., Hatton, C., De Waal, S., 1997. Link between the granitic and volcanic rocks of the Bushveld Complex, South Africa. J. Afr. Earth Sci. 95–104.
Sharpe, M., Bahat, D., Gruenewaldt, G., 1980. The Concentric Elliptical Structure of Feeder Sites to the Bushveld Complex and Possible Economic Implications. Research Report,. University of Pretoria, Institute For Geological Research On The Bushveld Complex.
Shithigona, O., Manzi, M., Ashwal, L.D., Bybee, G.M., Webb, S.J., 2018. Experimental studies of elastic wave velocities and densities in rocks from the Bushveld Complex, South Africa: implications for deep reflection seismic surveys. S. Afr. J. Geol. 121 (3), 311–326.
Smith, R., 1990. A review of stratigraphy and sedimentary environments of the Karoo Basin of South Africa. J. Afr. Earth Sci. 10 (1-2), 117–137.
Tugume, F., Nyblade, A., Julia, J., 2012. Moho depths and Poisson's ratios of Precambrian crust in East Africa: evidence for similarities in Archean and Proterozoic crustal structure, *Earth planet.* Sci. Lett. 355, 73–81.
Walraven, F., 1988. Notes on the age and genetic relationships of the Makhutso Granite, Bushveld Complex, South Africa. Chem. Geol. 17–28.
Webb, S.J., Cawthorn, R.G., Nguuri, T., James, D., 2004. Gravity modelling of Bushveld Complex connectivity supported by Southern African Seismic Experiment results. S. Afr. J. Geol. 107 (1–2), 207–218.
Webb, S.J., Ashwal, L.D., Cawthorn, R.G., 2011. Continuity between eastern and western Bushveld Complex, South Africa, confirmed by xenoliths from kimberlite. Contrib. Mineral. Petrol. 162, 101–107.
Willmore, C., Boudreau, A., Spivack, A., Kruger, F., 2002. Halogens of Bushveld Complex, South Africa δ37Cl and Cl/F evidence for hydration melting of the source region in a back-arc setting. Chem. Geol. 503–511.
Yang, Y., Li, A., Ritzwoller, M.H., 2008. Crustal and uppermost mantle structure in southern Africa revealed from ambient noise and teleseismic tomography. Geophys. J. Int. 175 (1), 235–248.
Youssof, M., Thybo, H., Artemieva, I., Levander, A., 2013. Moho depth and crustal composition in Southern Africa. Tectonophysics 609, 267–287.
Zeh, A., Ovtcharova, M., Wilson, A.H., Schaltegger, U., 2015. The Bushveld complex was emplaced and cooled in less than one million years - results of zirconology, and geotectonic implications. Earth Planet. Sci. Lett. 418, 103–114.
Zhu, L., Kanamori, H., 2000. Moho depth variation in southern California from teleseismic receiver functions. J. Geophys. Res. *10*5, 2969–2980.